Author's final version
Published as: *Nucl. Fusion* **61**, 126066 (2021)
https://doi.org/10.1088/1741-4326/ac36f2

Enhanced Particle Transport Events Approaching the Density Limit of the J-TEXT Tokamak

T. Long[1], P. H. Diamond[2*], R. Ke[1], L. Nie[1], M. Xu[1*], X. Y. Zhang[3], B. L. Li[1], Z. P. Chen[3], X. Xu[3], Z. H. Wang[1], T. Wu[1], W. J. Tian[1,4], J. B. Yuan[1], B.D. Yuan[1], S. B. Gong[1], C. Y. Xiao[1], J. M. Gao[1], Z. G. Hao[3], N. C. Wang[3], Z. Y. Chen[3], Z. J. Yang[3], L. Gao[3], Y. H. Ding[3], Y. Pan[3], W. Chen[1], G. Z. Hao[1], J. Q. Li[1], W. L. Zhong[1] and X. R. Duan[1]

[1] Southwestern Institute of Physics, Chengdu, China
[2] CASS and Department of Physics, University of California, San Diego, CA, USA
[3] International Joint Research Laboratory of Magnetic Confinement Fusion and Plasma Physics, State Key Laboratory of Advanced Electromagnetic Engineering and Technology, School of Electrical and Electronic Engineering, Huazhong University of Science and Technology, Wuhan, China
[4] Tsinghua University, Beijing, China

Email: longt@swip.ac.cn

Abstract

Enhanced particle transport events are discovered and analyzed as the density limit of the J-TEXT tokamak is approached. Edge shear layer collapse is observed and the ratio of Reynolds power to turbulence production decreases. Simultaneously, the divergence of turbulence internal energy flux (i.e. turbulence spreading) increases, indicating that shear layer collapse triggers an outward spreading event. Studies of correlations show that the enhanced particle transport events are quasi-coherent, and manifested primarily in density fluctuations which exhibit positive skewness. Electron adiabaticity emerges as the critical parameter which signals transport event onset. For $\alpha < 0.35$ as density approaches the Greenwald density, both turbulence spreading and density fluctuations rise rapidly. Taken together, these results elucidate the connections between edge shear layer, density fluctuations, particle transport events, turbulence spreading and plasma edge cooling as the density limit is approached.

Keyword: density limit, particle transport, shear flow, turbulence spreading

1. Introduction

High plasma density is favorable for fusion reactors, as fusion power is proportional to the square of plasma density. High density operation is considered as the baseline scenario for ITER[1] and DEMO[2]. However, the density limit imposes constraints on the maximum attainable density for current-generation tokamak operations[3]. The Greenwald empirical scaling shows that, the maximum central line-averaged density scales with plasma total current[4], i.e. $n_G(10^{20}\mathrm{m}^{-3}) = I_p(\mathrm{MA})/\pi a^2(\mathrm{m}^2)$.

There is a general agreement that the tokamak density limit is associated with progressive cooling of the plasma edge, leading to current shrinking and MHD instability, and ultimately disruption of the discharge[5]. A variety of mechanisms may cause edge cooling approaching the density limit, such as neutral effects, impurity radiation and plasma transport[5-7].

The decrease of the scrape-off layer transparency to neutrals, which is mainly due to charge exchange, lead to reduced fueling efficiency near the density limit on Frascati Tokamak Upgrade[8]. However, pellet fuelled discharges with peaked density profile manifested a limiting density to be 1.5-2 times the limit of those fuelled by gas puffing on Alcator C[3], JT-60[9], ASDEX[10], TFTR[11], DIII-D[12] and JET[13]. This suggests that fuelling itself is not responsible for the density limit described by n_G. In the impurity radiation model, the density limit is considered to occur when the radiation power exceeds the input power. This is not an entirely satisfactory explanation of some important observations, such as the frequent observation of radiation saturation at high density plasma, and the independence of attainable density on heating power and impurity content for discharges with Z_{eff} <2.5 [3, 14, 15].

The Greenwald limit is found to be closely associated with increased particle transport and particle confinement degration. The density relaxation time after pellet injection (a dynamic measure of particle confinement) decreases dramatically at $\bar{n} \sim n_G$ on Alcator C[3]. Increases in particle transport along with enhanced density fluctuations occurred in advance of MHD and radiation activity before density limit disruption on TEXT[16]. Similar phenomena were also obseverd in the experimental results in Alcator C-Mod[17]. Indeed, rapid transport events were found to restore the plasma to the limiting density without MHD activity of disruption, suggesting that particle transport is fundamental to the density limit phenomennology[4]. The key questions then are (i) what triggers such enhanced transport and (ii) what is the physics of the transport events.

Regarding question (i) above, edge fluctuation studies have linked such enhanced particle transport near the density limit to the collapse of the edge shear layer[18]. Note such edge shear layers are universal to tokamaks and stellarators[19-25]. Equivalently, long-range correlations—which are thought to be indicative of zonal flows—are observed to decrease rapidly at high density in the TEXTOR tokamak and the TJ-II stellarator[26]. For increasing collisionality leading to lower electron adiabaticity (i.e. lower α), the coupling between density and potential decreases, thus hindering the zonal flow drive, as shown on the TJ-K stellarator[27]. Electron adiabaticity parameter $\alpha = k_\parallel^2 v_{th,e}^2 / \nu_{ei}\omega$, where $k_\parallel$ is the parallel wavenumber, $v_{th,e}$ is the electron thermal speed, ν_{ei} is the electron-ion collision rate, and ω is the dominant frequency of turbulence. As the plasma response passes from adiabatic $(\alpha > 1)$ to hydrodynamic $(\alpha < 1)$, the Reynolds stress drive of the edge shear layer is reduced, and the particle flux is enhanced[18, 28, 29]. For the adiabatic regime, potential fluctuations and density fluctuations are closely coupled, and the plasma response is like that of a drift wave ($\tilde{n} \sim \tilde{\phi}$). For the hydrodynamic regime, potential fluctuations and density fluctuations are not simply proportional, and the plasma response is more like that of a convective cell. Previous theoretical work demonstrated a reduction in zonal flow production will occur when adiabaticity drops below unity[29]. Recent theoretical work indicates that the limiting edge density for shear layer collapse is predicted to scale with I_p, due to neoclassical screening of zonal flow[30]. We note here that other theoretical approaches have proposed a transition from drift wave to resistive ballooning mode turbulence as adiabaticity drops below unity as the origin of the enhanced particle transport at the density limit[31]. Note, however, that the distinction between "drift resistive ballooning mode" and "hydrodynamic collisional drift waves" is rather subtle and that discrimination is beyond the capability of the experiments of this paper. Also, the models proposed in [31] do not address shear layer collapse or its relation to the change in the state of the turbulence. As this is a primary focus of our paper, we do not discuss these alternative models further.

In this paper, we elucidate the physics of enhanced particle transport events as the density limit of the J-TEXT tokamak is approached. A reduction in the ratio of Reynolds power density to fluctuation power production as $\bar{n} \rightarrow n_G$ indicates that, the collapse of the shear layer is a consequence of reduced efficiency of zonal flow drive. Turbulence spreading was observed to occur and increase as the shear layer collapses, and the measurements suggest that the Reynolds power ultimately is channeled to turbulence spreading. Studies show that the transport event is quasi-coherent, with positively skewed density fluctuations, and manifested primarily as density structures. Electron adiabaticity emerges as the key parameter which signals the onset of particle transport events.

The remainder of this paper is organized as follows. Section 2 introduces the experimental set up. Section 3 presents the edge shear layer and turbulent particle flux measurements as $\bar{n} \rightarrow n_G$. Section 4 reports the kinetic and internal energy evolution. Section 5 reports the spreading dynamics of low-frequency density fluctuation events. Section 6 shows the emergence of adiabaticity as a key parameter as $\bar{n} \rightarrow n_G$. Section 7 presents conclusions.

2. Experimental set up

The experimental studies were conducted on the J-TEXT tokamak[32-35] with a limiter configuration. The major radius is 1.05m and the minor radius is 0.255m. The experiments were performed in Ohmic hydrogen discharges. The toroidal magnetic field B_t is ~ 1.6 / 1.9 /2.2 T . The plasma current I_p is ~ 130 / 150 / 190 kA, respectively. The edge safety factor q_a is ~ 3.8. The central line-averaged density $\bar{n}$ is (2.0-5.3) $\times\ 10^{19}\ \mathrm{m}^{-3}$. These discharges were carried out in one day, and the shot numbers ranged from 1070961 to 1071002. The maximum achievable density on J-TEXT is ~ 0.7 n_G. Here, n_G varies over ~6.4 / 7.3 / 9.3 $\times\ 10^{19}\ \mathrm{m}^{-3}$ for I_p ~ 130 / 150 / 190 kA respectively.

A specially designed reciprocating Langmuir probe array on the top port (13#) of the J-TEXT tokamak was used to perform the main experimental measurements. This is shown in Figure 1. The measurement coverage of this Langmuir probe is r = 24-28 cm, and its relative position to LCFS is $r - r_{LCFS} =$ [-1.5, 2.5] cm. The cylindrical probe tips are 2mm long with a diameter of 2mm. The separation between two adjacent tips is ~10 mm in the poloidal direction, ~2.5 mm in the radial direction, and ~5 mm in the toroidal direction, i.e. $d_\theta = 10$ mm, $d_r = 2.5$ mm, $d_\varphi =$ 5mm. Tip 9 and tip 10 compose one double probe. Tip 1 and tip 2 compose another double probe. A large and constant DC bias voltage (U_B~260 V) is applied between the two tips (i.e. negative tip and positive tip) of each double probe. The negative tip works in the ion saturation current regime. Thus, the current flow through the shunt resistor (R_s) in the circuit of double probe is ion saturation current, i.e. $I_{sat} = (V_- - V_+)/R_s$. Here, the potential on the upstream side of R_s is named V_-. The potential on the downstream side of R_s is named V_+. All the other tips are for floating potential measurements. Tip 8, 9, 10 compose a triple probe, which allows instantaneous measurements of electron temperature and electron density without voltage sweep[36, 37].

By using this probe, electron temperature T_e, plasma potential ϕ_p, electron density n, plasma $E \times B$ velocity, turbulent particle flux, turbulence intensity flux and turbulent Reynolds stress can be measured at the same time. The standard triple probe method was demonstrated to significantly overestimate electron temperature fluctuations at the edge of JET plasma[38]. Electron temperature fluctuations are in general difficult to measure and thus often neglected[21]. In our calculation, electron temperature fluctuations are ignored and therefore density and plasma potential fluctuations are inferred by the ion saturation current and floating potential fluctuations, respectively.

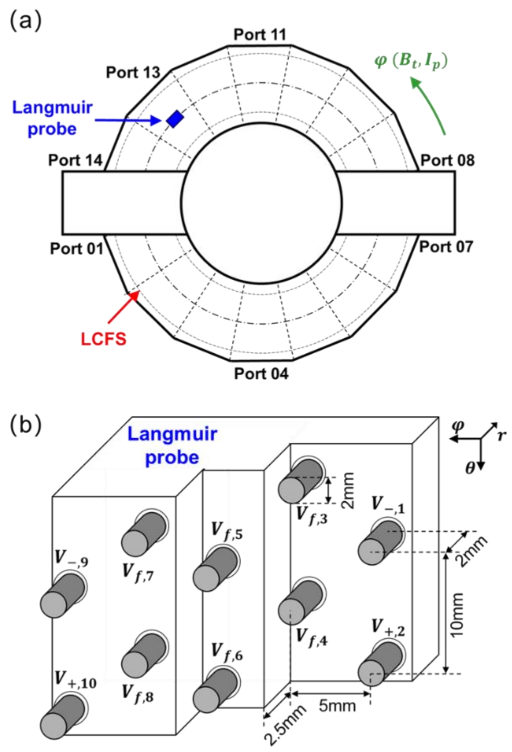

***Figure 1**. (a) Schematic top view of J-TEXT tokamak; (b) A reciprocating Langmuir probe array on the top port (13#) for the main experimental measurements*

Electron temperature is inferred by $T_e = (V_{+,10} - V_{f,8})/\ln 2$. Plasma potential is inferred by $\phi_p = V_{f,8} + 2.4T_e$. The $E \times B$ poloidal flow velocity is calculated as $v_{\theta,E\times B} = \nabla_r \phi_p / B_t$, which can be obtained from the radial profile measurement of ϕ_p by the reciprocation of probe. Ion saturation current on the top step of probe array is inferred by $I_{sat} = (V_{-,9} - V_{+,10})/R_s$. Ion saturation current on the bottom step of probe array is inferred by $I_{sat}^* = (V_{-,1} - V_{+,2})/R_s$. Electron density is inferred by $n_e = I_{sat}/(0.61eA_{eff}C_s)$, where C_s is ion sound speed and A_{eff} is the effective current collection area. The density fluctuation level is approximatively proportional to the ion saturation current fluctuation level in tokamak edge plasmas, i.e. $\tilde{I}_{sat}/\langle I_{sat}\rangle \sim \tilde{n}_e/\langle n_e\rangle$. Here, $\langle\cdot\rangle$ indicates a time average. With neglect of electron temperature fluctuations, the fluctuating radial velocity is inferred by the measured poloidal floating potential difference, $\tilde{v}_r = -\nabla_\theta \tilde{V}_f/B_t$. Similarly, the fluctuating poloidal velocity is inferred by the measured radial floating potential difference, $\tilde{v}_\theta = \nabla_r \tilde{V}_f/B_t$. The Reynolds stress $\langle \tilde{v}_r \tilde{v}_\theta \rangle$ is computed as $\langle (\tilde{V}_{f,5} - \tilde{V}_{f,6})(\tilde{V}_{f,4} - \tilde{V}_{f,8}) \rangle / (2 d_\theta d_r B_t^2)$. The turbulent particle flux $\langle \tilde{n} \tilde{v}_r \rangle$ is computed as $\langle \tilde{I}_{sat} (\tilde{V}_{f,7} - \tilde{V}_{f,8}) \rangle \langle n_e \rangle / (d_\theta B_t \langle I_{sat} \rangle)$. The turbulence intensity flux $\langle \tilde{n}^2 \tilde{v}_r \rangle$ is calculated as $\langle \tilde{I}_{sat}^2 (\tilde{V}_{f,7} - \tilde{V}_{f,8}) \rangle \langle n_e \rangle^2 / (d_\theta B_t \langle I_{sat} \rangle^2)$ [39]. All probe data was sampled at 2 MHz. A digital bandpass filter was applied to the data to obtain the fluctuations with a frequency range of 2-100 kHz. This filter is a zero-phase FIR filter with Hanning window. The filtering order is 2000.

Note that tips 1-6 of the probe array are shadowed in the toroidal direction by the probe skeleton. These measurements might be influenced by the shadowing effect and the toroidal flow change. Based on Langmuir probe principles[36, 40, 41], the relation between the collected upstream and downstream ion saturation current can be written as $I_{si,d} \cong I_{si,u} \exp(-M_\parallel/0.6)$. $M_\parallel = v_\parallel / C_s$ is the toroidal Mach number. For shadowed floating potential, $\phi_{f,shadowed} \cong \phi_{f,unshadowed} \left(1 + \frac{kT_e/e}{\phi_{f,unshadowed}} \ln \frac{2}{1+\exp\left(-\frac{M_\parallel}{0.6}\right)}\right)$. For shadowed ion saturation current, $I_{si,shadowed} \cong I_{si,unshadowed} (1 + \exp(-M_\parallel/0.6))^{-1}$. Unfortunately, the local measurement of $M_{\parallel}$ is not available in our experiments. Instead, we use Carbon V (CV) toroidal flow and ion temperature measurements from an ultraviolet spectrometer on J-TEXT[42] to make a rough estimation of this effect. It shows that the CV toroidal velocity is ~ -10 km/s (counter-current direction) at r~20 cm and nearly doesn't change as density increases from $0.32n_G$ to $0.63n_G$. The $M_{\parallel}$ of CV decreases from about -0.1 to -0.2 due to the decrease of temperature with the assumption of T_i~T_e . For $M_{\parallel}$ ~ [-0.2, -0.1], $\phi_{f,shadowed} \cong \phi_{f,unshadowed}(1 + \frac{kT_e/e}{\phi_{f,unshadowed}}[-0.18, -0.09])$. From probe measurements at the edge, $(kT_e/e)/\phi_{f,unshadowed}$ is ~ -0.5. Thus, the shadowed floating potential can be (approximately) regarded as equal to the unshadowed floating potential within a deviation level of ~ 10%. Meanwhile, $I_{si,shadowed} \cong I_{si,unshadowed}[0.41, 0.46]$. The shadowed ion saturation current is ~ 0.41-0.46 times smaller than the unshadowed ion saturation current. Note that this coefficient changes about 10% (i.e. from 0.46 to 0.41) as density increases from $0.32n_G$ to $0.63n_G$. Since the shadowed ion saturation current is only used to calculate the correlation and coherence between two $\tilde{I}_{sat}$ (in Section 5), the underestimated magnitude of ion saturation current is not expected to have a notable impact on the basic trend of the results for correlation and coherence.

3. Edge shear layer and turbulent particle flux

Figure 2(a-c) show radial profile evolutions of electron temperature, electron density and plasma potential respectively as the density approaches the Greenwald density. The black/blue/green/red curve represents the discharge with the central line-averaged density of 0.32/0.45/0.59/0.63 n_G, respectively. As $\bar{n}$ increases, edge temperature decreases, edge density increases at first but then saturates, and plasma potential decreases.

Benchmark with measurements from other diagnostics is helpful to make the results more convincing. Due to the different measurement locations and methods, the measurement results from Langmuir probe and other diagnostics are difficult to be compared quantitatively. Only qualitative comparisons can be made. Figure3(a) shows the evolution of electron density profile obtained by a far-infrared (FIR) polarimeter-interferometer (POLARIS) system [43] at a line-averaged density of 0.32/0.45/0.59/0.63 n_G. Here, negative r represents low-field-side, and positive r represents high-field-side. It shows that the edge density increases at first but then saturates as $\bar{n}$ increases. The density change trend measured by this POLARIS is consistent with the probe measurement, and the edge density value is also very close ($\sim 1.0 \times 10^{19} \mathrm{m}^{-3}$). Figure 3(b) shows the evolution of CV ion temperature profile obtained by a ultraviolet spectrometer[42]. Due to the fiber set up of this spectrometer, only three channels are available during our experiments. It shows that the edge CV ion temperature at $r \sim 20$ cm decreases as $\bar{n}$ increases. This is consistent with electron temperature evolution from probe measurement. The value of the edge ion temperature and the edge electron temperature are both about tens of eV. To sum up, the density and temperature measurements from other diagnostics are qualitatively consistent with those from the Langmuir probe.

An edge shear layer indicated by the $E \times B$ poloidal shear flow was found to exist in the edge region inside the LCFS (r =25.5cm), as shown by Figure 2(d). As $\bar{n}$ approaches n_G, both the edge poloidal flow velocity and its radial shearing rate decrease dramatically. The turbulent Reynolds stress decreases while the turbulent particle flux grows, as shown in Figure 2(e) and Figure 2(f) respectively.

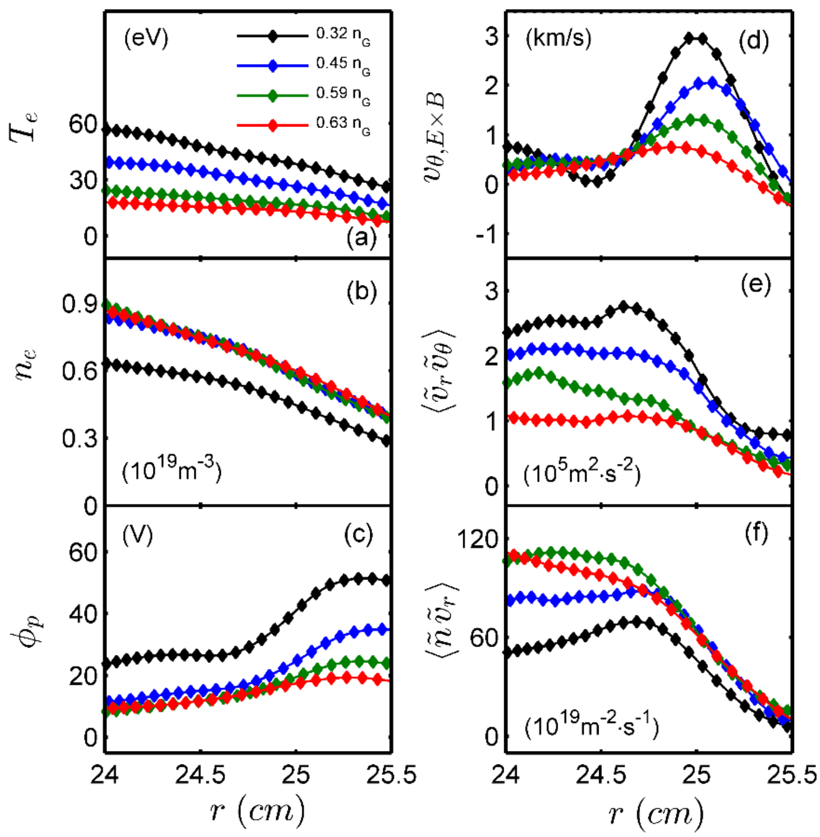

Figure 2. *(a) Electron temperature; (b) electron density; (c) plasma*

potential; (d) $E \times B$ poloidal velocity; (e) Reynolds stress; and (f) particle flux at a line-averaged density of 0.32/0.45/0.59/0.63 n_G

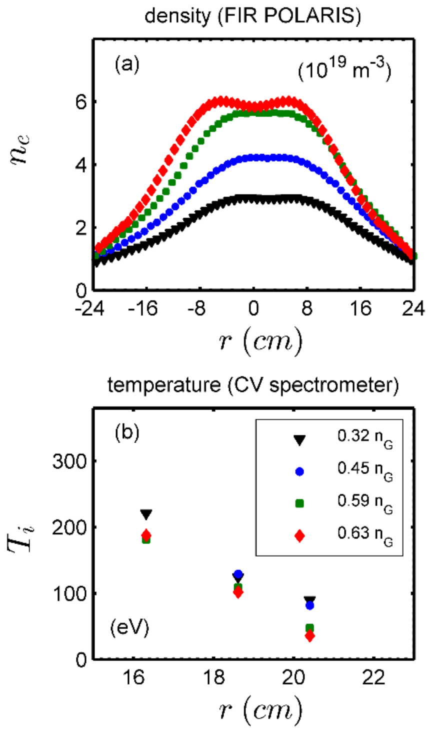

***Figure 3**. The radial profile of (a) electron density from FIR POLARIS; and (b) ion temperature of CV from ultraviolet spectrometer at a line-averaged density of 0.32/0.45/0.59/0.63 n_G*

Figure 4 shows the joint probability distribution function (joint PDF) of normalized radial velocity fluctuations and poloidal velocity fluctuations in the Reynolds stress. The joint PDF for density of $0.32\, n_G$ tilts more to the first and third quadrants (tilting degree ~45°) than for $0.63\, n_G$ (tilting degree ~15°). This indicates a decrease of symmetry breaking in the spectra of turbulence as line-averaged density increases from $0.32\, n_G$ to $0.63\, n_G$. Reduced symmetry breaking leads to decreased turbulence drive for edge poloidal flow. This is consistent with experimental results from the HL-2A tokamak[44], where the decreased spectral symmetry breaking in drift wave turbulence is in good agreement with the decreased poloidal flow and its torque in L mode discharges.

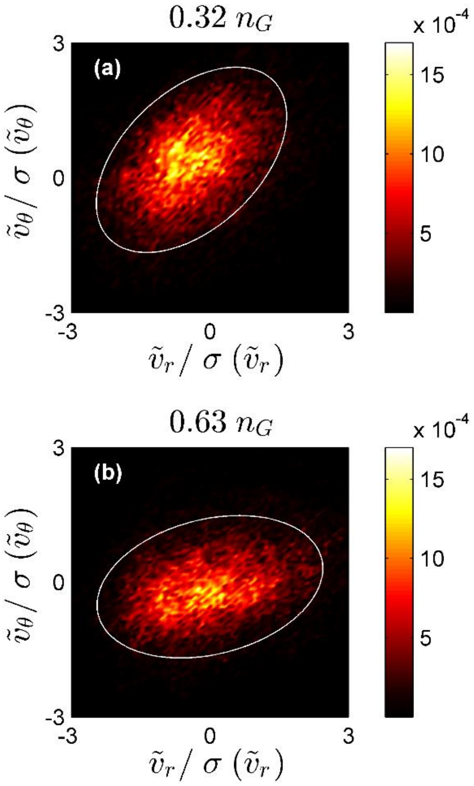

Figure 4. *The joint PDF of normalized radial velocity fluctuations and normalized poloidal velocity fluctuations at a line-averaged density of (a) 0.32* n_G*; (b) 0.63* n_G

4. Kinetic and internal energy evolution

A model framework is necessary in order to analyze the turbulence energetics as $\bar{n}$ approaches n_G. Following previous work[29, 30], we use the Hasegawa-Wakatani (H-W) system for collisional drift waves[45, 46]. This system is appropriate for density gradient driven turbulence in a collisional plasma, as at the edge of J-TEXT. The H-W system is fundamental and generic, and has a basic structure in common with other related reduced fluid models. Moreover, the model is used only to identify key power transfer terms, such as production power $\mathcal{P}_I$, Reynolds power $\mathcal{P}_K$ and spreading power $\mathcal{P}_S$. The analysis of the experimental data does not in any way depend upon evolving or solving the equations.

The basic equations are (1a) and (1b) for normalized $\tilde{n}$ and $\tilde{\phi}$ (i.e. $\tilde{n}/n_0$ and $e\tilde{\phi}/T$):

$$\left(\frac{\partial}{\partial t} + \vec{v}_E \cdot \nabla\right) \rho_s^2 \nabla_\perp^2 \tilde{\phi} = -\tilde{v}_r \frac{\partial}{\partial r} \rho_s^2 \langle \nabla_\perp^2 \tilde{\phi} \rangle - \chi_\parallel \nabla_\parallel^2 \rho_s^2 (\tilde{\phi} - \tilde{n}) + \mu \nabla_\perp^2 \rho_s^2 \nabla_\perp^2 \tilde{\phi} \tag{1a}$$

$$\frac{\partial}{\partial t} \tilde{n} + \vec{v}_E \cdot \nabla \tilde{n} = -\tilde{v}_r \frac{\partial}{\partial r} \langle n \rangle - \chi_\parallel \nabla_\parallel^2 (\tilde{\phi} - \tilde{n}) + D_n \nabla_\perp^2 \tilde{n} \tag{1b}$$

Here, $\chi_\parallel = k_\parallel^2 v_{the}^2 / \nu_e$ with $k_\parallel = 1/Rq$. For mean (i.e. poloidally and toroidally averaged) quantities:

$$\frac{\partial}{\partial t} \rho_s^2 \langle \nabla_r^2 \phi \rangle = -\frac{\partial}{\partial r} \langle \tilde{v}_r \rho_s^2 \nabla_r^2 \tilde{\phi} \rangle + \mu \nabla_r^2 \rho_s^2 \langle \nabla_r^2 \phi \rangle \tag{1c}$$

$$\frac{\partial}{\partial t} \langle n \rangle = -\frac{\partial}{\partial r} \langle \tilde{v}_r \tilde{n} \rangle + D_{n,0} \nabla_r^2 \langle n \rangle \tag{1d}$$

From Eqn. (1c) and (1d), the equations for the evolution of mean internal energy and mean kinetic energy follow directly. For mean internal energy $\langle E_I \rangle$:

$$\frac{\partial}{\partial t} \langle E_I \rangle = \frac{\partial}{\partial t} \int d^3x \frac{c_s^2 \langle n \rangle^2}{2} = \int d^3x \left[c_s^2 \langle \tilde{v}_r \tilde{n} \rangle \frac{\partial \langle n \rangle}{\partial r} - c_s^2 D_{n,0} \left(\frac{\partial \langle n \rangle}{\partial r} \right)^2 \right] \tag{2}$$

Here, the first term on the right-hand side (RHS) accounts for transfer of energy from the source $\nabla \langle n \rangle$ to fluctuations, i.e. the term is negative for production of turbulence energy. The second term accounts for diffusive dissipation. Endpoint contributions are ignored. Thus, from consideration of mean-fluctuation energy conservation, we have the net power density for production of fluctuations as:

$$\mathcal{P}_I = -c_s^2 \langle \tilde{v}_r \frac{\tilde{n}}{n_0} \rangle \frac{1}{n_0} \frac{\partial \langle n \rangle}{\partial r} \tag{3}$$

Note $\mathcal{P}_I > 0$ for a down gradient power, as for drift instability. $\langle \tilde{v}_r \tilde{n} \rangle$ is turbulent particle flux. Here, normalizations are explicit, for clarity. Likewise, for mean kinetic energy $\langle E_K \rangle$:

$$\frac{\partial}{\partial t} \langle E_K \rangle = \frac{\partial}{\partial t} \int \frac{\rho_s^2 c_s^2}{2} \langle \nabla_r \phi \rangle^2 \, d^3x = \int d^3x [\langle v_E \rangle' \langle \tilde{v}_r \tilde{v}_\theta \rangle - \frac{\mu \rho_s^2 c_s^2}{2} \langle \nabla_r^2 \phi \rangle^2] \tag{4}$$

Here, the first term on the RHS is net Reynolds power associated with the transfer of energy from the turbulence to the mean (i.e. zonal) flow. $\langle \tilde{v}_r \tilde{v}_\theta \rangle$ is the turbulent Reynolds stress and $\tilde{v}$ is supposed to be the $E \times B$ velocity. A positive first term means the zonal flow gains energy from the turbulence. The second term is simple viscous dissipation. Again, from consideration of mean-fluctuation energy conservation, we have the net power density for transfer from the turbulence to the zonal flow $\mathcal{P}_K$, i.e. Reynolds power:

$$\mathcal{P}_K = \langle \tilde{v}_r \tilde{v}_\theta \rangle \langle v_E \rangle' \tag{5}$$

Thus, we see that the ratio $\mathcal{P}_K / \mathcal{P}_I$ is a natural measure of the fraction of fluctuation power transferred to the zonal flow relative to fluctuation power produced by $\nabla \langle n \rangle$ relaxation. Then, a decrease in $\mathcal{P}_K / \mathcal{P}_I$ indicates a relative decline in the efficiency of zonal flow drive. Here,

$$\frac{\mathcal{P}_K}{\mathcal{P}_I} = \frac{\langle \tilde{v}_r \tilde{v}_\theta \rangle \partial_r \langle v_\theta \rangle}{-c_s^2 \langle \tilde{v}_r \tilde{n} \rangle \partial_r \langle n \rangle / \langle n \rangle^2} \tag{6}$$

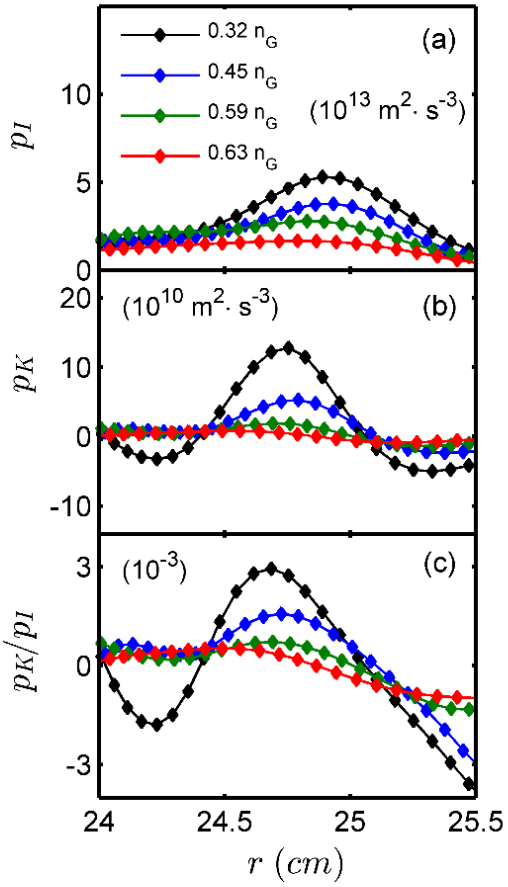

Figure 5. *(a) Production power $\mathcal{P}_I$; (b) Reynolds power $\mathcal{P}_K$; (c) dimensionless ratio $\mathcal{P}_K/\mathcal{P}_I$ at a line-averaged density of 0.32/0.45/0.59/0.63 n_G*

Figure 5(a) shows that the radial profile of the production power $\mathcal{P}_I$. $\mathcal{P}_I$ decreases as density approaches n_G. Figure 5(b) shows the radial profile of the Reynolds power $\mathcal{P}_K$. $\mathcal{P}_K$ also decreases as density approaches n_G. At relatively lower density (0.32/0.45 n_G), $\mathcal{P}_K$ is negative near the both sides of edge shear layer, which is consistent with previous experimental observations in the Ohmic plasmas of JET tokamak[47]. Figure 5(c) shows that the dimensionless ratio $\mathcal{P}_K/\mathcal{P}_I$

decreases significantly in the edge shear region as n/n_G increases. The peak value of $\mathcal{P}_K/\mathcal{P}_I$ drops by ~80% from 0.32 n_G to 0.63 n_G. This suggests that the shear layer collapse phenomenon observed in the high-density discharges is due to a reduction in the efficiency of energy transfer from edge turbulence to the poloidal $E \times B$ flow.

This study features novel results showing the evolution of "turbulence spreading" i.e. the divergence of the flux of turbulence internal energy, as density approaches n_G. To assess the contribution of spreading to fluctuation energetics, it is convenient to revisit energetics from the perspective of fluctuations rather than mean fields. Obviously, fluctuation and mean field enegetics are linked by energy conservation. For collisional drift wave turbulence, the total fluctuation energy density is the sum of kinetic plus internal pieces, i.e:

$$\varepsilon = \varepsilon_K + \varepsilon_I = \rho_s^2 c_s^2 \frac{\langle (\nabla\tilde{\phi})^2 \rangle}{2} + \frac{c_s^2}{2} \langle \left(\frac{\tilde{n}}{n_0}\right)^2 \rangle \tag{7a}$$

So the energy density flux Γ_ε is:

$$\Gamma_\varepsilon = \langle \tilde{v}_r \rho_s^2 c_s^2 \frac{(\nabla\tilde{\phi})^2}{2} \rangle + \langle \tilde{v}_r \frac{c_s^2}{2} \left(\frac{\tilde{n}}{n_0}\right)^2 \rangle \tag{7b}$$

Here, the first term on the RHS is the flux of kinetic energy density and the second term is the flux of internal energy density. We focus on the evolution of the latter as density approaches n_G, because the kinetic energy flux is two orders of magnitude smaller than the internal energy flux, and so is negligible. To compare spreading to production, we return to Eqn. (1a) to derive the turbulence internal energy density evolution equation:

$$\frac{\partial}{\partial t}\varepsilon_I + \frac{\partial}{\partial r}\langle \tilde{v}_r \varepsilon_I \rangle = \mathcal{P}_I - \chi_\parallel \frac{\tilde{n}}{n_0}\nabla_\parallel^2\left(\tilde{\phi} - \frac{\tilde{n}}{n_0}\right) - D_n \langle \frac{(\nabla_\perp \tilde{n})^2}{n_0^2} \rangle \tag{8}$$

Here ε_I is turbulence internal energy density. The second term is the divergence of the internal energy density flux due to spreading. $\mathcal{P}_I$ is given in Eqn. (3). The second RHS term reflects the dissipative coupling between $\tilde{\phi}$ and $\tilde{n}$ (intrinsic to collisional drift waves), and the last RHS term is diffusive dissipation. A natural measure of the fluctuation power increment due to spreading relative to that due to local production (i.e. input from the $\nabla\langle n \rangle$ source) is:

$$\frac{\mathcal{P}_S}{\mathcal{P}_I} = \frac{-\partial_r \langle \tilde{v}_r \varepsilon_I \rangle}{\mathcal{P}_I} = \frac{-\partial_r \langle \tilde{v}_r \tilde{n}^2 c_s^2 \rangle / 2n^2}{-\langle \tilde{v}_r \tilde{n} \rangle c_s^2 \partial_r \langle n \rangle / n^2} \tag{9}$$

Here, $\mathcal{P}_S < 0$ means that fluctuation internal energy is spreading out from the location, while $\mathcal{P}_S > 0$ means it is flowing in. An increase in $\mathcal{P}_S/\mathcal{P}_I$ means that the local internal power evolution is determined increasingly by spreading rather than by local production. Note that the spreading power $\mathcal{P}_S = -\partial_r \langle \tilde{v}_r \tilde{n}^2 c_s^2 \rangle / 2n^2$ here differs somewhat from the turbulence spreading term (the spreading of density fluctuation intensity) defined as $-\partial_r \langle \tilde{v}_r \tilde{n}^2 \rangle / 2$ in the reference[39].

Figure 6(a) presents the radial profile of turbulence production power $\mathcal{P}_I$ and Figure 6(b) presents the turbulence spreading power $\mathcal{P}_S$ as density approaches n_G. $\mathcal{P}_S$ is small (~0) for discharges with 0.32 n_G and becomes large for 0.63 n_G. Meanwhile, $\mathcal{P}_S$ tends to be increasingly negative in the region of $24 \text{ cm} < r < 24.9 \text{ cm}$ and increasingly positive in the region of $24.9 \text{ cm} < r < 25.5 \text{ cm}$ as density approaches n_G. This indicates enhanced outward turbulence spreading in high density discharges. Figure 6(c) shows that the dimensionless ratio of turbulence spreading to production $\mathcal{P}_S/\mathcal{P}_I$ increases dramatically as density approaches n_G. The peak value of $\mathcal{P}_S/\mathcal{P}_I$ increases by a factor of ~7 from 0.32 n_G to 0.63 n_G.

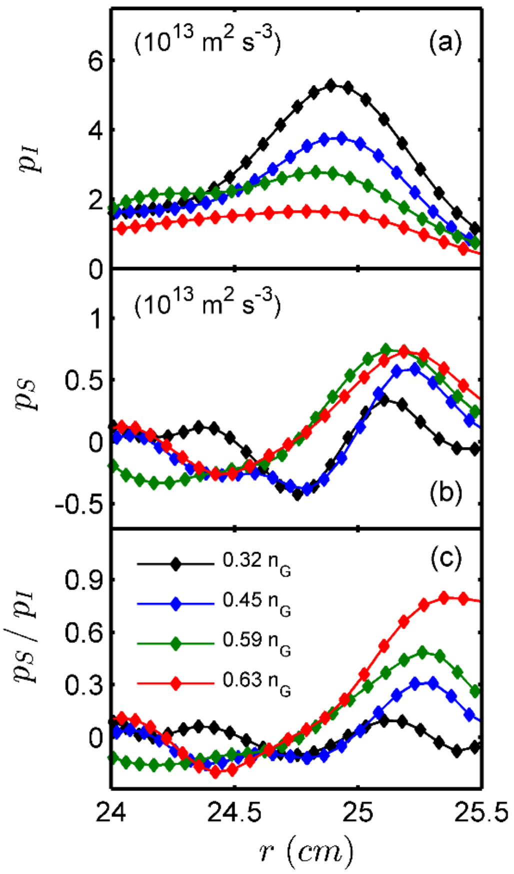

***Figure 6**. (a) Turbulence production power $\mathcal{P}_I$; (b) turbulence spreading power $\mathcal{P}_S$; (c) the dimensionless ratio $\mathcal{P}_S/\mathcal{P}_I$ at a line-averaged density of 0.32/0.45/0.59/0.63 n_G*

The relative turbulence energy change due to spreading $\mathcal{P}_S/\mathcal{P}_I$ increases while the relative Reynolds power ratio $\mathcal{P}_K/\mathcal{P}_I$ decreases. In fact, $(\mathcal{P}_K/\mathcal{P}_I)_{peak} * (\mathcal{P}_S/\mathcal{P}_I)_{peak} \sim 0.3/0.5/0.4/0.4 \times 10^{-3}$ within a range of line-averaged density of 0.32/0.45/0.59/0.63 n_G. Thus, $(\mathcal{P}_K/\mathcal{P}_I)_{peak} * (\mathcal{P}_S/\mathcal{P}_I)_{peak} \sim$const. This suggests that the energy is diverted from shear flow drive to outward spreading, as the shear layer collapses. Thus, turbulent particle transport increases as density approaches n_G.

5. Spreading dynamics – low-frequency density fluctuation events

Figure 7(a) shows the auto-spectra of ion saturation current fluctuations $\tilde{I}_{sat}$ in the edge region at $r \sim 25$ cm for the line-averaged density values of 0.32/0.45/0.59/0.63 n_G. Figure 7(b) shows the auto-spectra of radial velocity fluctuations. Here, $\tilde{v}_r$ is inferred by $(\tilde{V}_{f,7} - \tilde{V}_{f,8})/(d_\theta B_t)$. Figure 7(c) shows the auto-power spectra of normalized ion saturation current fluctuations $\tilde{I}_{sat}/I_{sat}$ and Figure 7(d) shows the auto-power spectra of normalized magnetic fluctuations $\tilde{B}_\theta/B$.

The low-frequency components (<50 kHz) of ion saturation current fluctuations increase as density approaches n_G. The low-frequency components (<50 kHz) of $\tilde{I}_{sat}/I_{sat}$ increase as density approaches n_G, while the high-frequency components (50-100 kHz) of $\tilde{I}_{sat}/I_{sat}$ don't change much. The low-frequency components (<50 kHz) of $\tilde{v}_r$ don't change much, and the high frequency components (50-100 kHz) of $\tilde{v}_r$ even decreases as density approaches n_G. Besides, there is almost no change in the cross phase[48] between density fluctuations and radial velocity fluctuations in the particle flux [49] as density approaches n_G. Therefore, these enhanced low-frequency density fluctuations contribute to the enhanced turbulent particle flux shown in Figure 2(f), and enhanced turbulence spreading shown in Figure 6(b). However, note that there is no obvious change in low-frequency, large scale MHD activity as density increases! Hence, we focus on the electrostatic fluctuation physics in our study of enhanced particle transport as density approaches n_G.

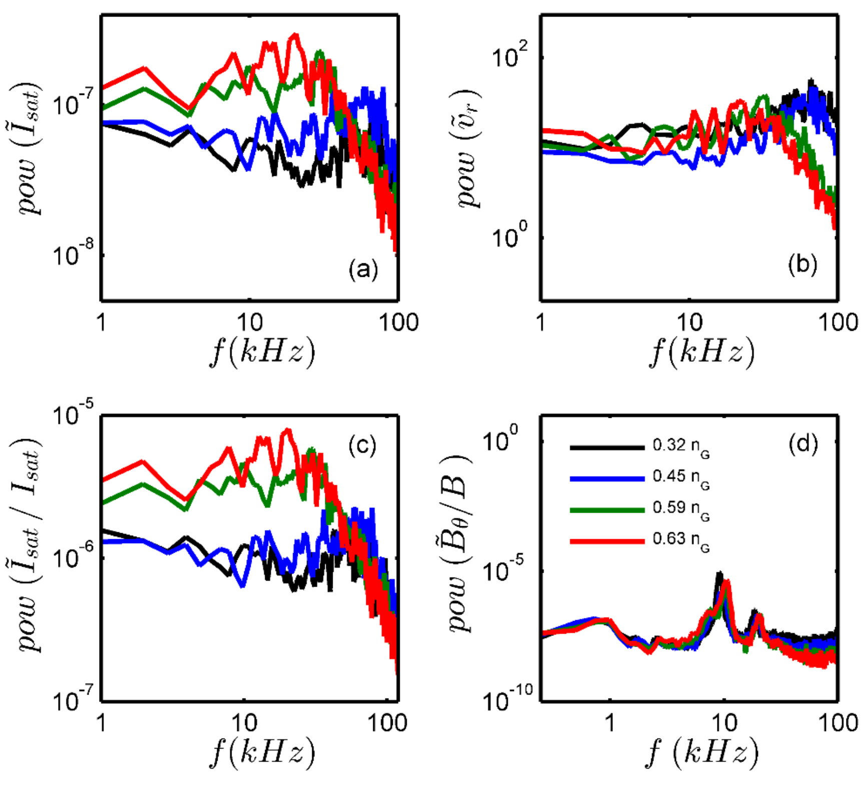

***Figure** 7. The auto-spectra of (a) ion saturation current fluctuations; (b) radial velocity fluctuations; (c) normalized ion saturation current fluctuations; and (d) normalized magnetic fluctuations at a line-averaged density of 0.32/0.45/0.59/0.63* n_G

Figure 8(a) presents the envelope of the auto correlation function of

$\tilde{I}_{sat}$ fluctuations at $r{\sim}25$ cm. Figure 8(b) shows the envelope of the auto correlation function of $\tilde{V}_f$ fluctuations at $r{\sim}25$ cm. The envelope of the auto correlation function is obtained from the absolute value of the Hilbert transform of the autocorrelation sequence. Thus, the auto correlation time τ_{ac} can be determined from the e-folding width of the envelope of auto correlation function[50]. τ_{ac} for $\tilde{I}_{sat}$ fluctuations increases as the line-averaged density increases. This is due to the fact that $\tilde{I}_{sat}$ fluctuation events have longer lifetime or the turbulence propagation velocity is reduced as $\bar{n}$ increases.

Figure 8(c) presents the envelope of the cross correlation function of two radially separated ion saturation current fluctuations at $r{\sim}25$ cm and $r{\sim}25.5$ cm. They are $\tilde{I}_{sat}$ on the top step of probe array and $\tilde{I}^*_{sat}$ on the bottom step of probe array, respectively. Figure 8(d) presents the envelope of the cross correlation function of two radially separated floating potential fluctuations ($\tilde{V}_{f,8}$ and $\tilde{V}_{f,4}$) at $r{\sim}25$ cm and $r{\sim}25.5$ cm. The cross correlation of radially separated $\tilde{I}_{sat}$ increases significantly as the line-averaged density increases, while the cross correlation of radially separated $\tilde{V}_f$ does not increase. This indicates that the enhanced, radially extended correlation exists in the density fluctuations but not in the potential fluctuations, as density increases.

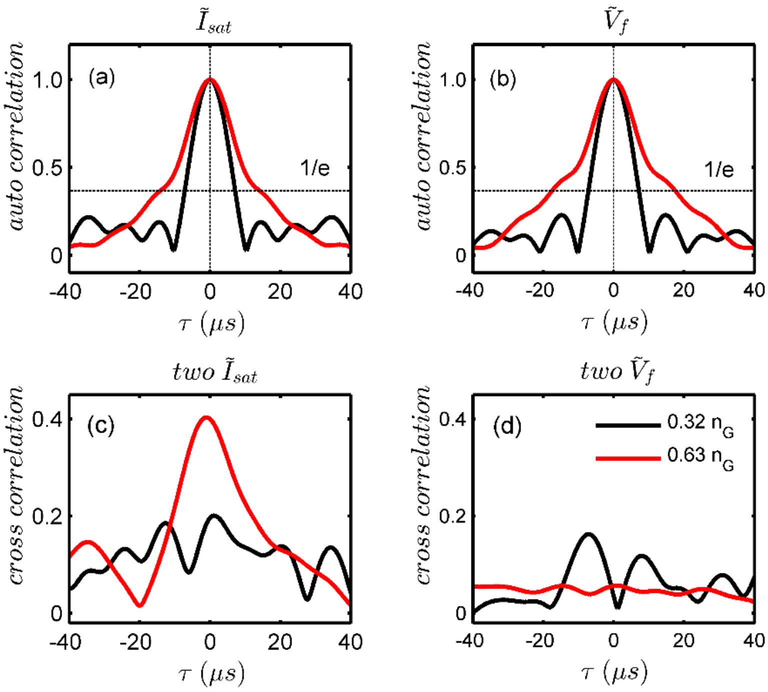

Figure 8. *The envelope of (a) auto correlation function of* $\tilde{I}_{sat}$*; (b) auto correlation function of* $\tilde{V}_f$*; (c) cross correlation function of two radially separated* $\tilde{I}_{sat}$*; (d) cross correlation function of two radially separated* $\tilde{V}_f$

Figure 9(a) and Figure 9(b) give the coherence and cross phase between two radially separated ion saturation current fluctuations ($\tilde{I}_{sat}$ and $\tilde{I}^{*}_{sat}$) at $r{\sim}25$ cm and $r{\sim}25.5$ cm. The coherence in the low-frequency range (2-50 kHz) increases as the line averaged density increases. The cross phase $\cos\phi$ is close to 1 in the low-frequency range (2-50 kHz) as $\bar{n}$ increases. This suggests that the radial correlation of low-frequency density fluctuations increases as $\bar{n}$ increases.

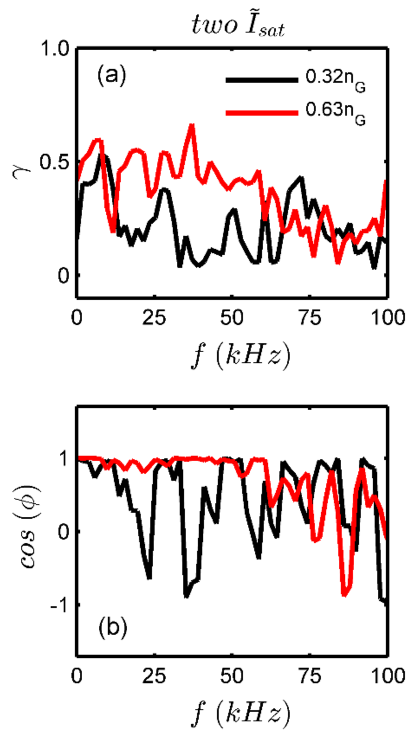

***Figure 9**. The (a) coherence and (b) cross phase between two radially separated* $\tilde{I}_{sat}$

The increase of low-frequency radial correlation and radial coherence in $\tilde{I}_{sat}$ is consistent with the interpretation of the occurrence of particle transport events. In this respect. these fluctuation measurements resemble those measured in flux driven simulations of turbulence, where extended correlation in pressure but not in potential[51] was observed. This is somewhat suggestive of avalanching. The experimental results here resemble small avalanches in density fluctuations on a scale of the edge shear layer. The onset of these small avalanches coincides with shear layer collapse as $\bar{n}$ approaches n_G.

Figure 10 shows the PDF of $\tilde{I}_{sat}$ at a line-averaged density of 0.32 n_G and 0.63 n_G. The skewness increases as $\bar{n}/n_G$ increases. The kurtosis of $\tilde{I}_{sat}$ fluctuations is unchanged. Note that a nearly symmetrical PDF evolves to a moderately skewed PDF due to the emergence of a more positively biased tail, which indicates $\tilde{n} > 0$ fluctuations predominate.

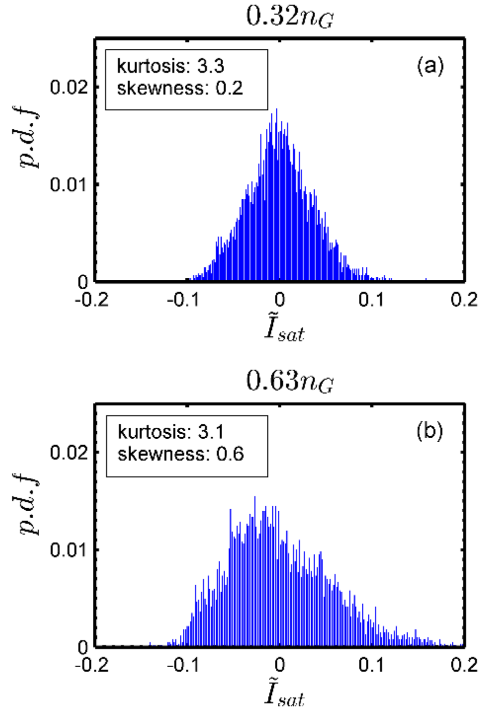

Figure 10. *The PDF characteristics of $\tilde{I}_{sat}$ at a line-averaged density of (a) 0.32 n_G; (b) 0.63 n_G*

6. Adiabaticity as a key parameter

Figure 11 shows the electron adiabaticity $\alpha = k_\parallel^2 v_{th,e}^2/(\nu_{ei}\omega)$ as a function of $\bar{n}/n_G$ for different I_p of ~ 130 / 150 / 190 kA. Here, $k_\parallel$ is estimated to be $\sim 1/qR$. As density approaches n_G, the electron adiabaticity decreases from $\alpha \sim 1$ to $\alpha \ll 1$, which suggests electrons enter the hydrodynamic regime. The $\alpha - \bar{n}/n_G$ curves for different plasma currents are very consistent. This shows that the transition of electron adiabaticity from the adiabatic regime ($\alpha > 1$) to hydrodynamic regime ($\alpha \ll 1$) is likely to be a common characteristic of high density discharges. The higher operational density available in discharges with higher plasma current is coincident with the evolution of electron adiabaticity.

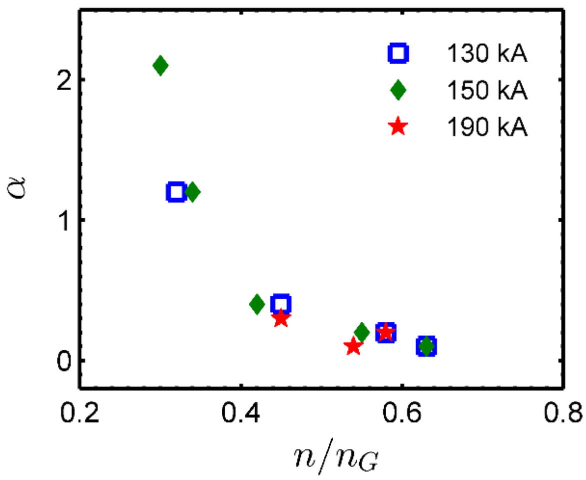

Figure 11. *Electron adiabaticity* α *VS* $\bar{n}/n_G$ *for different* I_p *of ~ 130 / 150 / 190 kA*

Figure 12(a) shows the $E \times B$ flow shearing rate as a function of α. Figure 12(b) shows the τ_{ac} for $\tilde{I}_{sat}$ fluctuations as a function of α. The $E \times B$ flow shearing rate decreases for $\alpha < 0.35$, while τ_{ac} for $\tilde{I}_{sat}$ increases at $\alpha < 0.35$. Figure 12(c) shows the normalized $\tilde{I}_{sat}$ amplitude as a function of α. Figure 12(d) shows the dimensionless ratio $\mathcal{P}_S/\mathcal{P}_I$ as a function of α. Both density fluctuation levels and the relative turbulence spreading strength rise for $\alpha < 0.35$. Adiabaticity emerges as a key parameter to determine the onset of edge shear layer collapse and enhanced particle transport events in high density discharges.

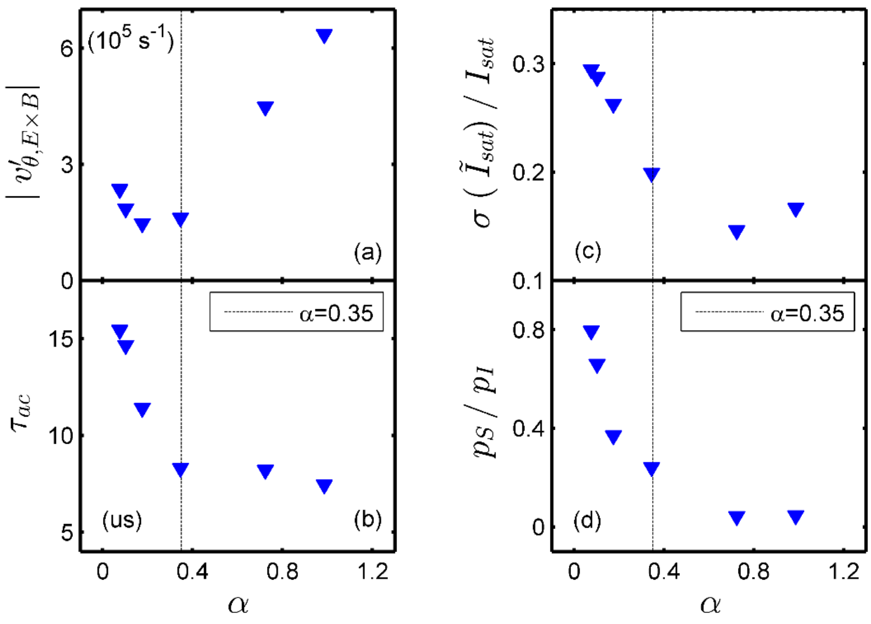

***Figure 12**. (a) $E \times B$ flow shearing rate; (b) auto correlation time of $\tilde{I}_{sat}$; (c) normalized $\tilde{I}_{sat}$ amplitude; and (d) dimensionless ratio of turbulence spreading $\mathcal{P}_S/\mathcal{P}_I$ as a function of electron adiabaticity α*

7. Conclusions

In this paper, we report the discovery and first analysis of enhanced particle transport events as the density approaches the density limit of the J-TEXT tokamak. Emphasis is on understanding the evolution and physics of the transport events. The principal results of this paper are:

(i) The observation of the collapse of the edge shear layer and an increase in particle flux as the density $\bar{n}$ approaches Greenwald density n_G.

(ii) The ratio of Reynolds power $\mathcal{P}_k$ to $\nabla\langle n\rangle$ driven fluctuation internal energy production power $\mathcal{P}_I$, i.e. $\mathcal{P}_K/\mathcal{P}_I$ drops as $\bar{n} \to n_G$. At the same time, the divergence of turbulence internal energy flux (i.e. turbulence spreading) rises relative to $\mathcal{P}_I$, i.e. $\mathcal{P}_S/\mathcal{P}_I$ increases. Note that $(\mathcal{P}_K/\mathcal{P}_I)_{peak} * (\mathcal{P}_S/\mathcal{P}_I)_{peak}$ is near constant as $\bar{n} \to n_G$. This suggests that shear layer collapse triggers turbulence spreading events. Instead of driving the turbulent Reynolds power, fluctuation power is channeled to turbulence spreading.

(iii) The auto-correlation time of $\tilde{I}_{sat}$ fluctuations (indicative of density fluctuations) increases as $\bar{n} \to n_G$. Likewise, the cross correlation of two radially separated $\tilde{I}_{sat}$ also increases. The skewness of $\tilde{I}_{sat}$ fluctuations is seen to be positive and increases as $\bar{n} \to n_G$, indicating $\tilde{n} > 0$ fluctuations predominate. Taken together, these observations indicate that the enhanced particle transport events are quasi-coherent and manifested primarily as density fluctuations. They have form of localized over-turning events or small "avalanches", since $\mathcal{P}_S$ transitions from < 0 to > 0 as radial location increases. This suggests outward transport of fluctuation energy. Magnetic fluctuations remain unchanged during the transport events.

(iv) Electron adiabaticity α emerges as the critical parameter which signals the onset of enhanced particle transport events. For $\alpha < 0.35$ as $\bar{n} \to n_G$, i.e. for which electrons enter the hydrodynamic regime, both spreading of fluctuation internal energy and density fluctuation level rise. τ_{ac} of $\tilde{I}_{sat}$ also increases as $\alpha < 0.35$, indicating increased coherency.

These results have several interesting implications, which we plan to explore in future experiments. First, previous results on tokamaks[52-54] observed a strengthening of the edge shear layer in L-mode, as auxiliary power is increased. Does that imply increased shear layer resilience to collapse at high density? This would be consistent with the basic scaling of $\alpha \sim T^2/n$ for drift wave turbulence, which suggest that increased edge temperature can enable increased edge density without shear layer collapse and enhanced transport. In macroscopic terms, these trends could identify the fluctuation physics underpinnings of a possible power or heat flux dependence of the density limit phenomenology. The latter is a topic of discussion, especially in the context of stellarators. However, caution is required here, and some care should be taken in distinguishing edge density from line averaged density. More generally, since the L-H transition power threshold P_{LH} increases with $\bar{n}$ at high density, a study of L-mode density limit physics would explore a space of power, such that $P/P_{LH} \leq 1$, and normalized density $\bar{n}/n_G \leq 1$ (at least). Exploration of the high power ($P/P_{LH} \rightarrow 1$) and high density $\bar{n}/n_G \rightarrow 1$ (or even beyond!) corner of this space would probe the dynamics of the competition between the L-H transition at high density and the density limit physics, and so be of great interest in the context of ITER operation scenarios development.

Future work on this subject will also include studies of current dependency of the dynamics, with emphasis on $\mathcal{P}_K$, $\mathcal{P}_I$, $\mathcal{P}_S$ scaling, and that of particle diffusion and density fluctuations. Meanwhile, it is worthwhile to compare the experimental result with relevant theoretical work[30]. Besides, nonlinear poloidal momentum flux [25], which is significant to poloidal rotation drive in strong turbulence, is planned to be studied experimentally. The physics regarding the particle transport events in the edge plasma (inside LCFS) and SOL plasma could be very different since the magnetic field lines are open in the SOL. Turbulent transport behavior in the SOL is very interesting and will be studied further in future. We also aim to understand better the structure of the density avalanches[55] and how they might interact with radiative condensation processes, and edge cooling. In particular, we speculate here that the formation of a large "slug" of density by the edge transport event could seed radiative condensation instabilities at the plasma edge. These could then trigger the familiar chain of events, i.e. Marfe → current profile contraction→MHD→disruption. In a related vein, a particle transport event could also trigger edge cooling by entrainment of colder particles, neutrals, etc.

Acknowledgments

The authors would like to acknowledge discussions with R. J. Hong, L. Wang, C. Hidalgo, M. Greenwald, N. Fedorczak, A. M. Garofalo, G. R. Tynan and C. S. Shen. We have benefitted greatly from the First Chengdu Theory Festival 2018 and the Festival de Théorie 2019, where many relevant topics were discussed. This work is supported by: the National

Key R&D Program of China under Grant No. 2018YFE0303100, 2017YFE0301201 and 2018YFE0310300; the National Natural Science Foundation of China under Grant No. 11905050, U1867222, 11875124, 11875023, 51821005 and 11905080; the Sichuan Youth Science and Technology Innovation Team Project under Grant No. 2020JDTD0030; the SWIP Artificial Sun Program under Grant No. 202001XWCXRZ004. The work is also supported by the U.S. Department of Energy, Office of Science, Office of Fusion Energy Sciences under Award Number DE-FG02-04ER54738.

References

[1] DOYLE E J, HOULBERG W A, KAMADA Y, et al. Chapter 2: Plasma confinement and transport [J]. Nuclear Fusion, 2007, 47(6): S18.

[2] ZOHM H, ANGIONI C, FABLE E, et al. On the physics guidelines for a tokamak DEMO [J]. Nuclear Fusion, 2013, 53(7): 073019.

[3] GREENWALD M, TERRY J L, WOLFE S M, et al. A new look at density limits in tokamaks [J]. Nuclear Fusion, 1988, 28(12): 2199.

[4] MARTIN G. Density limits in toroidal plasmas [J]. Plasma Physics and Controlled Fusion, 2002, 44(8): R27.

[5] GREENWALD M, BADER A, BAEK S, et al. 20 years of research on the Alcator C-Mod tokamak [J]. Phys Plasmas, 2014, 21(11): 110501.

[6] BORRASS K. Disruptive tokamak density limit as scrape-off layer/divertor phenomenon [J]. Nuclear Fusion, 1991, 31(6): 1035-51.

[7] WESSON J A, GILL R D, HUGON M, et al. Disruptions in JET [J]. Nuclear Fusion, 1989, 29(4): 641-66.

[8] FRIGIONE D, PIERONI L, ZANZA V, et al. High density operation on Frascati Tokamak Upgrade [J]. Nuclear Fusion, 1996, 36(11): 1489-99.

[9] KAMADA Y, HOSOGANE N, YOSHINO R, et al. Study of the density limit with pellet fuelling in JT-60 [J]. Nuclear Fusion, 1991, 31(10): 1827-33.

[10] STABLER A, MCCORMICK K, MERTENS V, et al. Density limit investigations on ASDEX [J]. Nuclear Fusion, 1992, 32(9): 1557-83.

[11] BELL M G, SCHMIDT G L, EFTHIMION P C, et al. Attainment of high plasma densities in TFTR with injection of multiple deuterium pellets [J]. Nuclear Fusion, 1992, 32(9): 1585-91.

[12] MAINGI R, MAHDAVI M A, PETRIE T W, et al. Density limit studies on DIII-D [J]. Journal of Nuclear Materials, 1999, 266-269(598-603.

[13] LANG P T, ALPER B, BAYLOR L R, et al. High density operation at JET by pellet refuelling* [J]. Plasma Physics and Controlled Fusion, 2002, 44(9): 1919-28.

[14] PETRIE T W, KELLMAN A G, MAHDAVI M A. Plasma density limits during Ohmic L mode and ELMing H mode operation in DIII-D [J]. Nuclear Fusion, 1993, 33(6): 929-54.

[15] RAPP J, VRIES P C D, SCH LLER F C, et al. Density limits in TEXTOR-94 auxiliary heated discharges [J]. Nuclear Fusion, 1999, 39(6): 765-76.

[16] BROWER D L, YU C X, BRAVENEC R V, et al. Confinement degradation and enhanced microturbulence as long-time precursors to high-density-limit tokamak disruptions [J]. Physical Review Letters, 1991, 67(2): 200-3.

[17] LABOMBARD B, BOIVIN R L, GREENWALD M, et al. Particle transport in the scrape-off layer and its relationship to discharge density limit in Alcator C-Mod [J]. Phys Plasmas, 2001, 8(5): 2107-17.

[18] HONG R, TYNAN G R, DIAMOND P H, et al. Edge shear flows and particle transport near the density limit of the HL-2A tokamak [J]. Nuclear Fusion, 2018, 58(1): 016041.

[19] SHESTERIKOV I, XU Y, TYNAN G R, et al. Experimental Evidence for the Intimate Interaction among Sheared Flows, Eddy Structures, Reynolds Stress, and Zonal Flows across a Transition to Improved Confinement [J]. Physical Review Letters, 2013, 111(5): 055006.

[20] ALONSO J A, VELASCO J L, AR VALO J, et al. Dynamics of zonal-flow-like structures in the edge of the TJ-II stellarator [J]. Plasma Physics and Controlled Fusion, 2012, 55(1): 014001.

[21] TYNAN G R, XU M, DIAMOND P H, et al. Turbulent-driven low-frequency shearedE×Bflows as the trigger for the H-mode transition [J]. Nuclear Fusion, 2013, 53(7): 073053.

[22] XU M, TYNAN G R, DIAMOND P H, et al. Frequency-Resolved Nonlinear Turbulent Energy Transfer into Zonal Flows in Strongly Heated L-Mode Plasmas in the HL-2A Tokamak [J]. Physical Review Letters, 2012, 108(24): 245001.

[23] HIDALGO C, PEDROSA M A, GARC A L, et al. Experimental evidence of coupling between sheared-flow development and an increase in the level of turbulence in the $\mathrm{TJ}\text{\ensuremath{-}}\mathrm{II}$ stellarator [J]. Physical Review E, 2004, 70(6): 067402.

[24] GRENFELL G, VAN MILLIGEN B P, LOSADA U, et al. The impact of edge radial electric fields on edge–scrape-off layer coupling in the TJ-II stellarator [J]. Nuclear Fusion, 2019, 60(1): 014001.

[25] WANG L, WEN T, DIAMOND P H. Poloidal rotation driven by nonlinear momentum transport in strong electrostatic turbulence [J]. Nuclear Fusion, 2016, 56(10): 106017.

[26] XU Y, CARRALERO D, HIDALGO C, et al. Long-range correlations and edge transport bifurcation in fusion plasmas [J]. Nuclear Fusion, 2011, 51(6): 063020.

[27] SCHMID B, MANZ P, RAMISCH M, et al. Collisional Scaling of the Energy Transfer in Drift-Wave Zonal Flow Turbulence [J]. Physical Review Letters, 2017, 118(5): 055001.

[28] WANG L, TYNAN G R, HONG R, et al. Edge turbulence evolution and intermittency development near the density limit on the HL-2A tokamak [J]. Phys Plasmas, 2019, 26(9): 092303.

[29] HAJJAR R J, DIAMOND P H, MALKOV M A. Dynamics of zonal shear collapse with hydrodynamic electrons [J]. Phys Plasmas, 2018, 25(6): 062306.

[30] SINGH R, DIAMOND P H. Bounds on edge shear layer persistence while approaching the density limit [J]. Nuclear Fusion, 2021, 61(7): 076009.

[31] ROGERS B N, DRAKE J F, ZEILER A. Phase Space of Tokamak Edge Turbulence, the $\mathit{L}\ensuremath{-}\mathit{H}$ Transition, and the Formation of the Edge Pedestal [J]. Physical Review Letters, 1998, 81(20): 4396-9.

[32] LIANG Y, WANG N C, DING Y H, et al. Overview of the recent experimental research on the J-TEXT tokamak [J]. Nuclear Fusion, 2019, 59(11): 112016.

[33] ZHUANG G, PAN Y, HU X, et al. The reconstruction and research progress of the TEXT-U tokamak in China [J]. Nuclear Fusion, 2011, 51(9): 094020.

[34] DING Y, CHEN Z, CHEN Z, et al. Overview of the J-TEXT progress on RMP and disruption physics [J]. Plasma Science and Technology, 2018, 20(12): 125101.

[35] SHI P, ZHUANG G, GENTLE K, et al. First time observation of local current shrinkage during the MARFE behavior on the J-TEXT tokamak [J]. Nuclear Fusion, 2017, 57(11): 116052.

[36] CHEN S L, SEKIGUCHI T. Instantaneous Direct-Display System of Plasma Parameters by Means of Triple Probe [J]. Journal of Applied Physics, 1965, 36(8): 2363-75.

[37] QAYYUM A, AHMAD N, AHMAD S, et al. Time-resolved measurement of plasma parameters by means of triple probe [J]. Review of Scientific Instruments, 2013, 84(12): 123502.

[38] SILVA C, GON ALVES B, HIDALGO C, et al. Fluctuation measurements using a five-pin triple probe in the Joint European Torus boundary plasma [J]. Review of Scientific Instruments, 2004, 75(10): 4314-6.

[39] MANZ P, RIBEIRO T T, SCOTT B D, et al. Origin and turbulence spreading of plasma blobs [J]. Phys Plasmas, 2015, 22(2): 022308.

[40] CHEN F F. Langmuir probe diagnostics; proceedings of the Mini-Course on Plasma Diagnostics, IEEEICOPS meeting, Jeju, Korea, F, 2003 [C].

[41] HUTCHINSON I H. Principles of Plasma Diagnostics: Second Edition [J]. Plasma Physics and Controlled Fusion, 2002, 44(12): 2603-.

[42] CHENG Z F, LUO J, WANG Z J, et al. Edge impurity rotation profile measurement by using high-resolution ultraviolet/visible spectrometer on J-TEXT [J]. Review of Scientific Instruments, 2014, 85(11): 11E423.

[43] CHEN J, ZHUANG G, LI Q, et al. High resolution polarimeter-interferometer system for fast equilibrium dynamics and MHD instability studies on Joint-TEXT tokamak (invited) [J]. Review of Scientific Instruments, 2014, 85(11): 11D303.

[44] LONG T, DIAMOND P H, XU M, et al. Studies of Reynolds stress and the turbulent generation of edge poloidal flows on the HL-2A tokamak [J]. Nuclear Fusion, 2019, 59(10): 106010.

[45] HASEGAWA A, WAKATANI M. Plasma Edge Turbulence [J]. Physical Review Letters, 1983, 50(9): 682-6.

[46] WAKATANI M, HASEGAWA A. A collisional drift wave description of plasma edge turbulence [J]. The Physics of Fluids, 1984, 27(3): 611-8.

[47] S NCHEZ E, HIDALGO C, GON ALVES B, et al. On the energy transfer between

flows and turbulence in the plasma boundary of fusion devices [J]. Journal of Nuclear Materials, 2005, 337-339(296-300.

[48] BOEDO J A, TERRY P W, GRAY D, et al. Suppression of Temperature Fluctuations and Energy Barrier Generation by Velocity Shear [J]. Physical Review Letters, 2000, 84(12): 2630-3.

[49] LONG T. Experimental studies of edge shear layer in proximity to the density limit of the J TEXT tokamak [M]. Asia Pacific Transport Working Group Meeting & US EU Transport Task Force Workshop. Online. 2021.

[50] YAN Z, XU M, DIAMOND P H, et al. Intrinsic Rotation from a Residual Stress at the Boundary of a Cylindrical Laboratory Plasma [J]. Physical Review Letters, 2010, 104(6): 065002.

[51] CARRERAS B A, NEWMAN D, LYNCH V E, et al. A model realization of self-organized criticality for plasma confinement [J]. Phys Plasmas, 1996, 3(8): 2903-11.

[52] YAN Z, MCKEE G, FONCK R, et al. Observation of the L− H Confinement Bifurcation Triggered by a Turbulence-Driven Shear Flow in a Tokamak Plasma [J]. Physical review letters, 2014, 112(12): 125002.

[53] SCHMITZ L. The role of turbulence–flow interactions in L- to H-mode transition dynamics: recent progress [J]. Nuclear Fusion, 2017, 57(2): 025003.

[54] KIM E-J, DIAMOND P H. Zonal Flows and Transient Dynamics of the \$L\mathrm{\text{\ensuremath{-}}}H\$ Transition [J]. Physical Review Letters, 2003, 90(18): 185006.

[55] HAHM T S, DIAMOND P H. Mesoscopic Transport Events and the Breakdown of Fick's Law for Turbulent Fluxes [J]. Journal of the Korean Physical Society, 2018, 73(6): 747-92.